

# Injectable tissue prosthesis for instantaneous closed-loop rehabilitation

<https://doi.org/10.1038/s41586-023-06628-x>

Received: 9 August 2022

Accepted: 8 September 2023

Published online: 1 November 2023

 Check for updates

Subin Jin<sup>1,2,8</sup>, Heewon Choi<sup>2,3,8</sup>, Duhwan Seong<sup>2,3</sup>, Chang-Lim You<sup>4</sup>, Jong-Sun Kang<sup>4</sup>,  
Seunghyok Rho<sup>5</sup>, Won Bo Lee<sup>5</sup>, Donghee Son<sup>2,3,6</sup> & Mikyung Shin<sup>1,2,7</sup>✉

To construct tissue-like prosthetic materials, soft electroactive hydrogels are the best candidate owing to their physiological mechanical modulus, low electrical resistance and bidirectional stimulating and recording capability of electrophysiological signals from biological tissues<sup>1,2</sup>. Nevertheless, until now, bioelectronic devices for such prostheses have been patch type, which cannot be applied onto rough, narrow or deep tissue surfaces<sup>3–5</sup>. Here we present an injectable tissue prosthesis with instantaneous bidirectional electrical conduction in the neuromuscular system. The soft and injectable prosthesis is composed of a biocompatible hydrogel with unique phenylborate-mediated multiple crosslinking, such as irreversible yet freely rearrangeable biphenyl bonds and reversible coordinate bonds with conductive gold nanoparticles formed in situ by cross-coupling. Closed-loop robot-assisted rehabilitation by injecting this prosthetic material is successfully demonstrated in the early stage of severe muscle injury in rats, and accelerated tissue repair is achieved in the later stage.

Advances in closed-loop gait rehabilitation integrated with lighter-weight exoskeletons and wearable or implantable devices have substantially improved the quality of patient healthcare owing to the potential for clinical effectiveness originating from efficient recovery of motor and sensory malfunctions associated with severely injured nervous and muscular systems<sup>6,7</sup>. Despite such progress, achieving early-stage recovery of locomotion remains challenging. In this regard, the application of an electroconductive hydrogel strategy used in rapid tissue repair to the conventional soft tissue prosthesis approach may resolve such unmet needs owing to the low electrical impedance, mechanical modulus match, tissue adhesion and even biodegradability of hydrogels. Such hydrogels satisfy essential requirements for electrophysiological tissue conduction in the early stage of rehabilitation, effective low-threshold electrical stimulation to organ surfaces for accelerated tissue regeneration and recording of low-noise physiological signals for closed-loop healthcare systems, enabling precise diagnosis and feedback treatment<sup>1–3,8–11</sup>.

So far, most tissue-interfacing bioelectronics used in neuroprostheses have been based on the patch-type formfactor and are limited in their ability to access cramped, complicated and tiny biological interfaces in injured tissue regions<sup>3–5</sup>. On the other hand, syringe-injectable and conductive hydrogels have progressed in recent years and can be effectively introduced into inaccessible sites for tissue engineering and in the soft bioelectronics field<sup>12–15</sup>. However, most injectable and/or conductive materials with dynamic reversible bonds (for example, host–guest interactions, hydrogen bonds) that simply have embedded electroconductive additives show low mechanical and electrical durability because of their weak molecular bonds and heterogeneous

electrical percolation by poor gelation, thereby undesirably impeding long-term stable on-site tissue interfacing<sup>16–18</sup>. Although strong irreversible covalent bonds can be introduced to enhance the mechanical properties of the existing hydrogels<sup>19</sup>, they often cause a trade-off with the injectability of those materials.

Here we report injectable tissue-interfacing prostheses composed of conductive hydrogels (termed IT-IC hydrogels) generated via phenylborate (PB)-mediated multiple crosslinking strategies. The IT-IC hydrogels contain irreversible biphenyl bonds (Fig. 1a(i), red dashed box), reversible strong coordinate bonds between conductive gold nanoparticles (AuNPs) in situ reduced by biphenyl coupling and PB groups (green dashed box), and weak multivalent ionic interactions such as hydrogen bonds, metal- $\pi$  bonds and metal–carboxylate ( $\text{Au}^{3+}$ – $\text{COO}^-$ ) interactions on polysaccharide backbones. The PB-derived multiple bonds synergistically allow effective energy dissipation through both dissociation of weak noncovalent bonds and biphenyl rearrangement under shear stress during injection (Fig. 1a(ii)) and self-recovery after injection (Fig. 1a(iii)), which are entirely differentiated from those of the typical noninjectable hydrogels with irreversible covalent bonds, which inevitably lead to mechanical failure (Supplementary Fig. 1). Furthermore, electrically conductive AuNPs, ionically conductive polymers and numerous free ions (for example,  $\text{Na}^+$  and  $\text{Au}^{3+}$ ) synergistically confer electrical percolation within the network. This combinatorial crosslinking mechanism provides highly conformal and electrophysiological interfacing capability to the hydrogels, allowing simultaneous function as either tissue-to-tissue conduction through filling muscle-tissue loss for immediate rehabilitation in the early stage and accelerated myofibre regeneration in the long-term stage (Fig. 1b, red dashed box)

<sup>1</sup>Department of Intelligent Precision Healthcare Convergence, Sungkyunkwan University, Suwon, Republic of Korea. <sup>2</sup>Center for Neuroscience Imaging Research, Institute for Basic Science, Suwon, Republic of Korea. <sup>3</sup>Department of Electrical and Computer Engineering, Sungkyunkwan University, Suwon, Republic of Korea. <sup>4</sup>Department of Molecular Cell Biology, Single Cell Network Research Center, School of Medicine, Sungkyunkwan University, Suwon, Republic of Korea. <sup>5</sup>School of Chemical and Biological Engineering, Institute of Chemical Processes, Seoul National University, Seoul, Republic of Korea. <sup>6</sup>Department of Superintelligence Engineering, Sungkyunkwan University, Suwon, Republic of Korea. <sup>7</sup>Department of Biomedical Engineering, SKKU Institute for Convergence, Sungkyunkwan University, Suwon, Republic of Korea. <sup>8</sup>These authors contributed equally: Subin Jin, Heewon Choi. ✉e-mail: daniel3600@g.skku.edu; mikyungshin@g.skku.edu

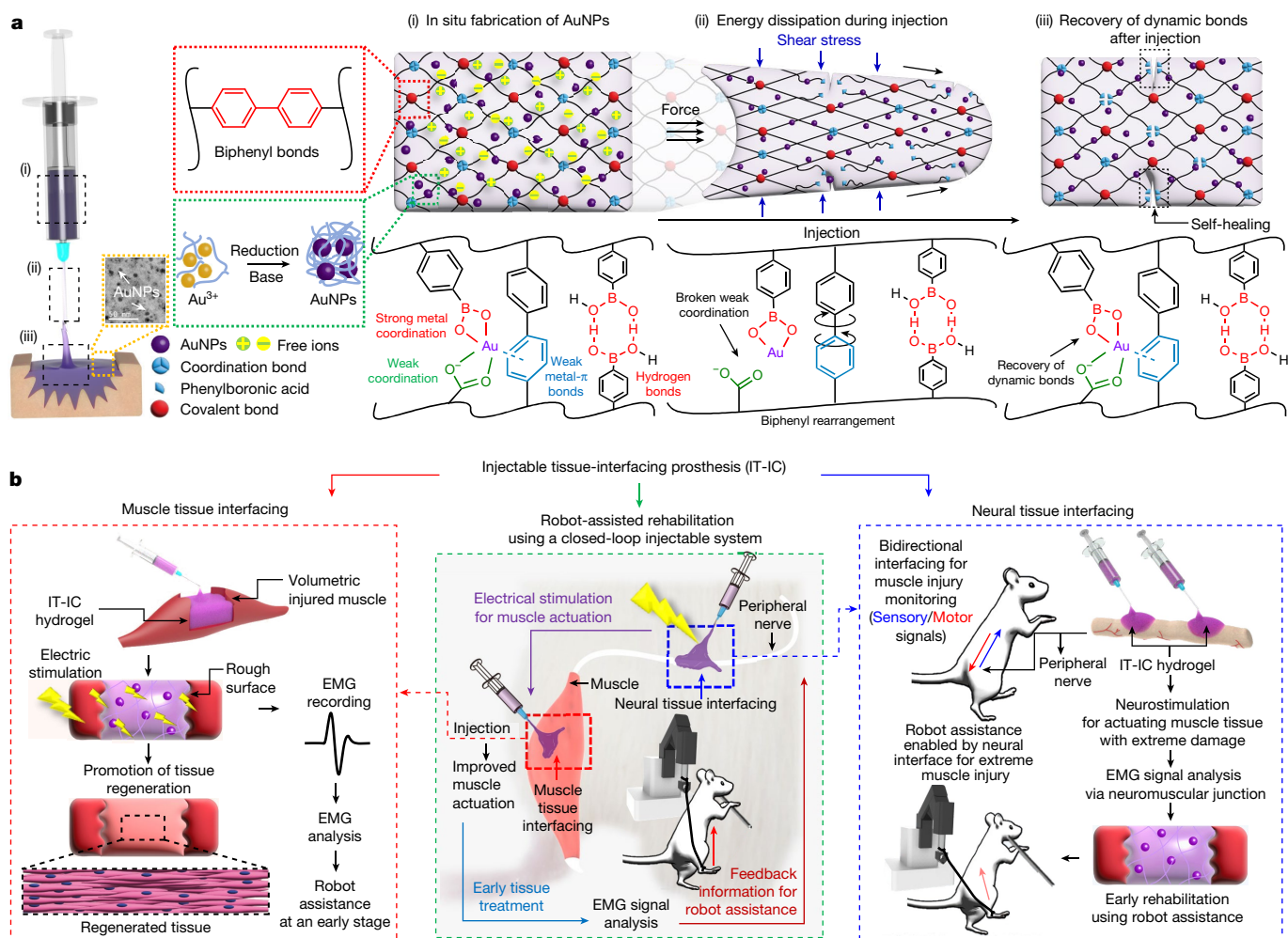


**Fig. 1 | Design of an injectable tissue prosthesis (IT-IC hydrogel) and its interfacing applications. a**, Schematic illustration of the molecular mechanism for the injectability of the IT-IC hydrogel. **b**, Description of

C-RAR (green dashed box) achieved by filling the injured muscle (red dashed box) or nerve (blue dashed box) with IT-IC hydrogel and further tissue repair.

or tissue-to-bioelectronics bridging for bidirectional stimulation and recording of peripheral nerves (blue dashed box). Specifically, such transfer of electrical signals generated from the muscle can be aided by robotic rehabilitation that is precisely controlled by a closed-loop system capable of peripheral nerve stimulation and feedback electromyogram (EMG) monitoring and vice versa (green dashed box).

### Characterization of IT-IC hydrogels

To prepare the IT-IC hydrogels, PB-tethered hyaluronic acid (HA-PB) was synthesized via a carbodiimide coupling reaction, and the degree of PB conjugation ( $\text{DOC}_{\text{PB}}\%$ ) was set to  $10.0 \pm 0.3\%$  (HA-PB<sub>high</sub>) (Supplementary Fig. 2a,b)<sup>20</sup>. To achieve a desirable mechanical modulus of the hydrogels for further in vivo implantation, we chose a crosslinking mechanism for the in situ conductive gelation of HA-PB solution containing Au(III) ions that was triggered by adding sodium hydroxide (NaOH) (Fig. 2a), which is a type of modified Suzuki-Miyaura reaction using palladium catalysts<sup>21</sup>. Under mildly basic conditions (approximately pH 9), PB groups undergo ionization, deboronation and transmetalation catalysed by in situ Au(III) reduction (Fig. 2a)<sup>22</sup>. Simultaneously, the phenyl carbanions formed by deboronation are covalently crosslinked to each other (for example, by biphenyl homocoupling), generating IT-IC hydrogels. The details of the IT-IC hydrogel gelation mechanism are provided in Supplementary Fig. 3 and

Supplementary Note 1. The gelation depends on a stoichiometric ratio of [NaOH] to [Au(III) ions], and a ratio of 4 formed the IT-IC hydrogel with the highest storage modulus ( $G' = 188.9 \pm 28.3$  Pa at 1 Hz) and the lowest loss factor ( $\tan \delta = 0.018 \pm 0.003$ ) within 1 min (Fig. 2b, Supplementary Fig. 4 and Supplementary Note 2). Other variables, such as  $\text{DOC}_{\text{PB}}\%$ , polymer concentration, the NaOH/Au<sup>3+</sup> ratio, amount of Au<sup>3+</sup>, and types of metal catalyst and solvent, can affect rheological properties regarding the stiffness and injectability of the IT-IC hydrogels (Supplementary Figs. 5–8 and Supplementary Note 3). In addition, the diameter and size distribution of AuNPs in situ formed in the hydrogels depended on the NaOH/Au<sup>3+</sup> ratio (Supplementary Fig. 9 and Supplementary Note 4). Considering the storage moduli of the soft biological tissues (around 0.1–400 kPa)<sup>23,24</sup>, IT-IC hydrogels consisting of 2 wt% HA-PB<sub>high</sub> crosslinked at a NaOH/Au<sup>3+</sup> ratio of 4 (termed IT-IC@4) were chosen for the following experiments and used after stabilization of the polymeric crosslinking and sufficient gold reduction through overnight incubation at room temperature.

The formation of biphenyl rings and AuNPs within the IT-IC hydrogel network was detected by Fourier transform infrared (FT-IR) spectroscopy (Fig. 2c) and X-ray photoelectron spectroscopy (XPS) (Supplementary Fig. 10 and Supplementary Note 5). In the FT-IR spectra of the lyophilized IT-IC@4 and IT-IC@1 (NaOH/Au<sup>3+</sup> ratio = 1), new peaks appeared at  $1,535\text{ cm}^{-1}$  (Fig. 2c, blue) and  $1,550\text{ cm}^{-1}$  (red), respectively, indicating C–C stretching vibration in biphenyl rings<sup>25</sup>. In addition,

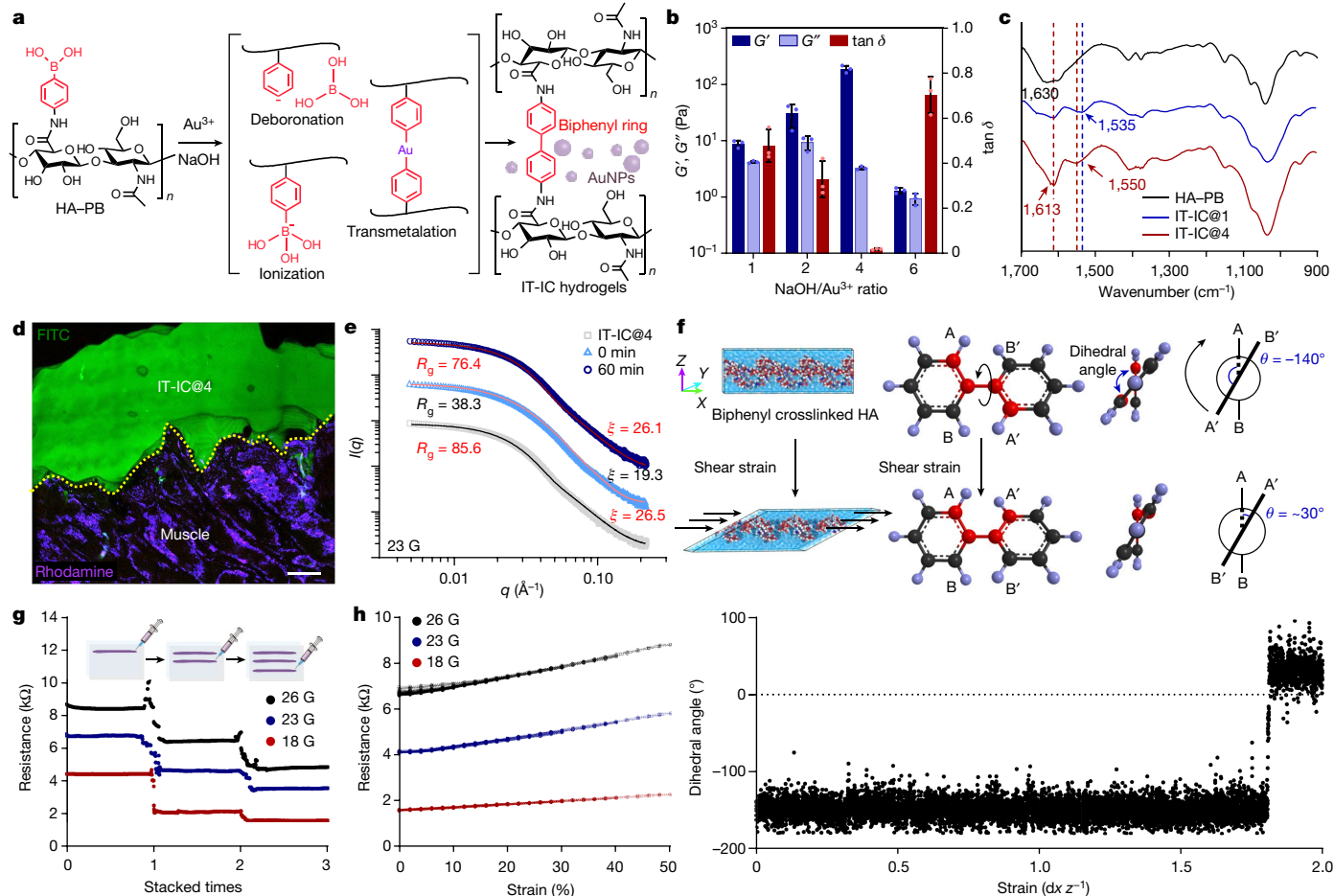


**Fig. 2 | Physicochemical and electrical characterization of the IT-IC hydrogel.**

**a**, The gelation mechanism of IT-IC hydrogel via the PB-derived biphenyl homocoupling reaction. **b**, Storage moduli ( $G'$ ) (blue), loss moduli ( $G''$ ) (light blue), and  $\tan \delta$  (red) values (mean  $\pm$  s.d.;  $n = 3$  for independent samples) of IT-IC hydrogel consisting of HA-PB<sub>high</sub> as a function of the NaOH/Au<sup>3+</sup> ratio. **c**, FT-IR spectra of HA-PB alone (black), IT-IC@1 (blue) and IT-IC@4 (red). **d**, On-tissue conformal contact capability of IT-IC@4 (green) encapsulating fluorescein isothiocyanate (FITC) on skeletal muscle tissue (purple) stained with rhodamine. The yellow dashed line indicates the edge of the tissue. Scale bar, 1 mm. **e**, Small-angle X-ray scattering patterns for scattering intensity,  $I(q)$ , of IT-IC@4 as a function of scattering vector,  $q$ , before injection (grey), and the hydrogel

filament immediately after injection with a 23 G needle (light blue) and at 60 min after injection (dark blue). **f**, Computational MD simulation of rotational rearrangement of the biphenyl rings during shear deformation. Strain was calculated as  $dx$  (changed length in  $x$ -axis direction) per  $z$  (length in  $z$ -axis direction). **g**, Changes in electrical resistance of the IT-IC hydrogel filament extruded with different needles (26 (black), 23 (blue) and 18 G (red)) with each stacked three times. The dimensions of the filament (area  $\times$  length) are  $0.39\pi \text{ mm}^2 \times 20 \text{ mm}$  for 26G,  $5.24\pi \text{ mm}^2 \times 20 \text{ mm}$  for 23G, and  $12.46\pi \text{ mm}^2 \times 20 \text{ mm}$  for 18G. **h**, Electrical hysteresis curve of the IT-IC hydrogel injected during the stretching–releasing test under 0, 10, 20, 30, 40 and 50% strain.

the peak at  $1,630 \text{ cm}^{-1}$  that appeared in the spectrum of HA-PB corresponded to the C=O stretching vibration of amide bonds (Fig. 2c, black), yet there was a sharp peak at  $1,613 \text{ cm}^{-1}$  only for IT-IC@4, demonstrating the formation of a large number of AuNPs<sup>26</sup>. In the high-resolution XPS spectra of the hydrogels, an increase in C–C bonds by the formation of biphenyl rings, a decrease in C–B bonds by deboronation and fabrication of AuNPs were clearly shown (Supplementary Fig. 10 and Supplementary Note 5).

As mentioned above, the PB-derived multiple crosslinking strategies, including reversible strong or weak coordinate bonds aided by rearrangeable biphenyl bonds, allow great injectability of IT-IC@4, which corresponds to the rapid shear thinning behaviour (Supplementary Fig. 6b) and self-healing properties of the hydrogels (Supplementary Fig. 11). On the basis of its rheological properties, IT-IC@4 also exhibited excellent conformal contact when applied to rough surfaces of damaged biological tissues (for example, muscle) or three-dimensional (3D) curved objects by injection using needles with different inner diameters (for example, 260  $\mu\text{m}$  for 26 gauge (G) and 838  $\mu\text{m}$  for 18G

(Fig. 2d, yellow dashed line and Supplementary Fig. 12), demonstrating their benefit as stable interfacing materials on biotic and abiotic substrates. Regarding the injectability and on-tissue conformability of the IT-IC hydrogels, we hypothesized that the configurational change of the hydrogel network occurs spontaneously during or after injection owing to dynamic strong or weak coordinate bonds. To test this hypothesis, we performed small-angle X-ray scattering analysis (Fig. 2e). The scattering pattern of the IT-IC hydrogels before injection was fitted to the Gel Fit model in SasView<sup>27,28</sup> (Fig. 2e, square), where the correlation length ( $\xi$ ), which refers to the distance between the polymer bundles or chains in the network, was calculated to be 26.5, and the gyration radius ( $R_g$ ) of the polymer bundle was 85.6. Notably, the pattern of the hydrogel filaments immediately after injection (0 min) showed a low  $\xi$  value of 19.3 and an  $R_g$  value of 38.3 (Fig. 2e, triangle), indicating that the physical distance between the polymer bundles or single polymers becomes shorter owing to the disruption of weak coordinate bonds after high shear stress. By contrast, at 1 h after injection, these values had recovered, with  $\xi = 26.1$  and  $R_g = 76.4$

(Fig. 2e, circle), indicating the structural recovery of the polymer bundle in the hydrogel filaments by reassociation of the coordinate bonds. In addition, the rotational rearrangement of the biphenyl rings during shear deformation was detected through a computational molecular dynamics (MD) simulation (Fig. 2f and Supplementary Note 6). The dihedral angle of the rings abruptly changed from  $-140^\circ$  to  $+30^\circ$  when the strain exceeded 1.8 (Fig. 2f, red-coloured balls in the middle and right graph). For further discussion, we compared the oscillation amplitude behaviour, stress relaxation behaviour and cyclic compressive stress–strain curves of IT-IC hydrogels with those of typical hydrogels crosslinked by alkane C–C bonds (Supplementary Fig. 13 and Supplementary Note 7). These results suggest that dissociation of multiple dynamic bonds enables great injectability and shape-morphing conformability of the IT-IC hydrogels, and rotational rearrangements of biphenyl rings at threshold strain might support these mechanical characteristics.

To investigate the electrical performance of IT-IC@4 in the neuromuscular system, we monitored whether the resistance of bulk IT-IC@4 was reversible without electrical hysteresis when the strain increased to 100% (Supplementary Fig. 14a–c). In addition, its impedance (0.68 k $\Omega$  at 1 kHz) and phase were stable in the stretching mode with 30% strain, and charge storage capacity (3.73 mC cm $^{-2}$ ) at 30% strain was comparable to that at 0% strain (3.74 mC cm $^{-2}$ ) (Supplementary Fig. 15). This might be because elasticity of the IT-IC hydrogel leads to an increase in the exposed polymer surface and enhances charge transport at the interface between the polymer and electrolytes. The charge storage capacity was also maintained after 50 cycles and there was no significant difference in the impedance value of the hydrogels even after applying 1,000 pulses of stimulation (peak-to-peak voltage ( $V_{pp}$ ) = 1 V). Further results for electrical resistance of the IT-IC hydrogels with a smaller number of AuNPs are described in Supplementary Fig. 16 and Supplementary Note 8. Similar to those of bulk hydrogels, the hydrogel filaments of IT-IC@4 injected through needles (26, 23 or 18G) possessed stable electrical resistance (of around several kilohms) that decreased with each stack of the filament (Fig. 2g, inset scheme). That is, electrical flow can pass through the IT-IC@4 filaments continuously. Although a gradual increase in the resistance of the filaments injected using 26 or 23G needles was observed as a function of strain (Supplementary Fig. 14d and Fig. 2h, black and blue), the resistance of the 18G filament was stable overall under 50% strain (red). In particular, in stretching and releasing tests under 0, 10, 20, 30, 40 and 50% strain, the electrical hysteresis of the hydrogel filaments (23 and 18G) was negligible, and their resistance values were reversibly recovered after deformation. However, slight hysteresis for the thin filament extruded by 26G needles was detected because of rapid dehydration. These stable and reversible electrical properties of IT-IC@4 result from the synergistic effect of both freely rearrangeable biphenyl bonds with delocalized electrons and conductive AuNPs. When the hydrogel is stretched, the rearrangement of biphenyl rings can help to prevent a certain degree of internal cracking in the hydrogels, but spatially distant AuNPs decrease the conductivity. After release, the electrical resistance of the hydrogel recovers to the original value owing to the strain resistance of the hydrogel crosslinked by PB.

These findings suggest that PB-derived biphenyl bonds and AuNPs in situ generated by cross-coupling reactions allow homogeneous gelation with injectability and strain-resistant electrical properties for further interfacing of implantable bioelectronics. Comparing the performance of most injectable and conductive hydrogels crosslinked via noncovalent bonds (for example, hydrogen bonds, ionic bonds,  $\pi$ – $\pi$  interactions) and encapsulation of conductive additives (for example, polypyrrole, graphene oxide and gold nanorods) (Supplementary Fig. 17), the IT-IC hydrogels satisfy important requirements for soft tissue prosthesis, tissue-like conductivity ( $10^{-2}$  S cm $^{-1}$ ), injectability using a needle with a small aperture (around 260  $\mu$ m) and conformability on rough and curved areas.

## Muscle-to-IT-IC hydrogel interfacing

Compared with the organ attachment methodology of conventional film-type bioelectrical patches, the injectability of our IT-IC hydrogel makes it capable of interfacing seamlessly with narrow and/or deep difficult-to-reach tissues injured by diverse events, such as surgical operations, traumatic injury and congenital or acquired anomalies<sup>29</sup>. Before the following biological tests, we investigated the in vitro dissociation profile of IT-IC@4, which showed swelling behaviour in physiological conditions over 2 days and slow dissociation for 5 days, releasing AuNPs (Supplementary Fig. 18). As a tissue-interfacing material, the biocompatibility of the IT-IC hydrogels was sufficient to maintain around 99% viability of two different neuron-like cells (differentiated PC12 and HT22 cells) treated with the hydrogel releasates (Supplementary Fig. 19). In addition, we confirmed ex vivo electrical conduction capability of the IT-IC hydrogel (Supplementary Fig. 20). The electrical signals were successfully transferred from one stimulated muscle through IT-IC to another muscle to be recorded, and the EMG amplitude (2.2 mV) was highest with IT-IC@4 interfacing when compared with that of other controls. To better clarify the capacity of IT-IC hydrogels for in vivo tissue–tissue conduction, we applied IT-IC hydrogels to a muscle injury model established by cross-sectional cutting of the whole tissue, which causes complex and rough surfaces of the damaged tissues as well as irrecoverable damage, potentially interfering with the recognition of precisely intended motions, which is a key requirement for performing early-stage closed-loop robot-assisted rehabilitation (C-RAR)<sup>30</sup> (Fig. 3 and Supplementary Fig. 21). Under electrical stimulation of the muscle around a proximal region of the sciatic nerve, electrophysiological functional recovery (EMG amplitude) of the muscle tissue was immediately detected on stacking each IT-IC hydrogel filament (50  $\mu$ l) using a 26G needle (Fig. 3a and Supplementary Video 1). The EMG amplitude ( $25.7 \pm 0.6$  mV) of IT-IC hydrogels with a total of 350  $\mu$ l (bulk or injected filaments) on the damaged tissues is comparable with that of pristine normal muscle tissue ( $31.7 \pm 3.4$  mV) (Fig. 3b). The recording of EMG signals indicates that viscous IT-IC hydrogels with a thin filament formfactor can conformally contact the damaged interfaces and stably allow electrical flow between the tissues. Such instantaneous electrophysiological functional recovery was notably different from that of a control group without the injection of IT-IC hydrogels when electrical stimulation was applied from 0.1 V to 10 V (Fig. 3c). Moreover, the IT-IC hydrogel could be used as a surface electrode capable of directly recording the EMG signals from the muscle tissue (Supplementary Fig. 22). These results demonstrate that even after injection, the IT-IC hydrogel enables effective tissue conduction and ultra-conformable contact at the tissue–hydrogel interfaces without areal loss, owing to its reversible conductivity based on biphenyl-driven AuNP formation and modulus matching to that of muscle, respectively.

Recent reports suggest that implantation of conductive scaffolds helps myogenic differentiation by efficient electrical conduction<sup>31,32</sup>. Thus, filling the defect region with IT-IC hydrogels can promote myogenesis and myoblast proliferation through the effective charge storage capability of the hydrogel even in the absence of cells or growth factors. After induction of volumetric muscle loss (VML) injury (diameter, 8 mm), treatment with IT-IC hydrogel could successfully regenerate the muscle tissue within 4 weeks (Fig. 3d). In histological analysis through haematoxylin and eosin (H&E) staining, IT-IC@4 significantly increased the number of centrally nucleated myofibres compared with non-treated and gelatin-methacryloyl (Gel-MA)-treated groups at 1 and 2 weeks (Figs. 3e,g and Supplementary Note 9). After 4 weeks, the high aspect ratio of the myofibres demonstrates enhanced myofibre growth induced by the hydrogels (Figs. 3f,h). The implanted IT-IC@4 exhibited gradual degradation, generated a mild immune response and showed acceptable long-term biocompatibility, as evidenced by the low fibrotic tissue area and infiltration

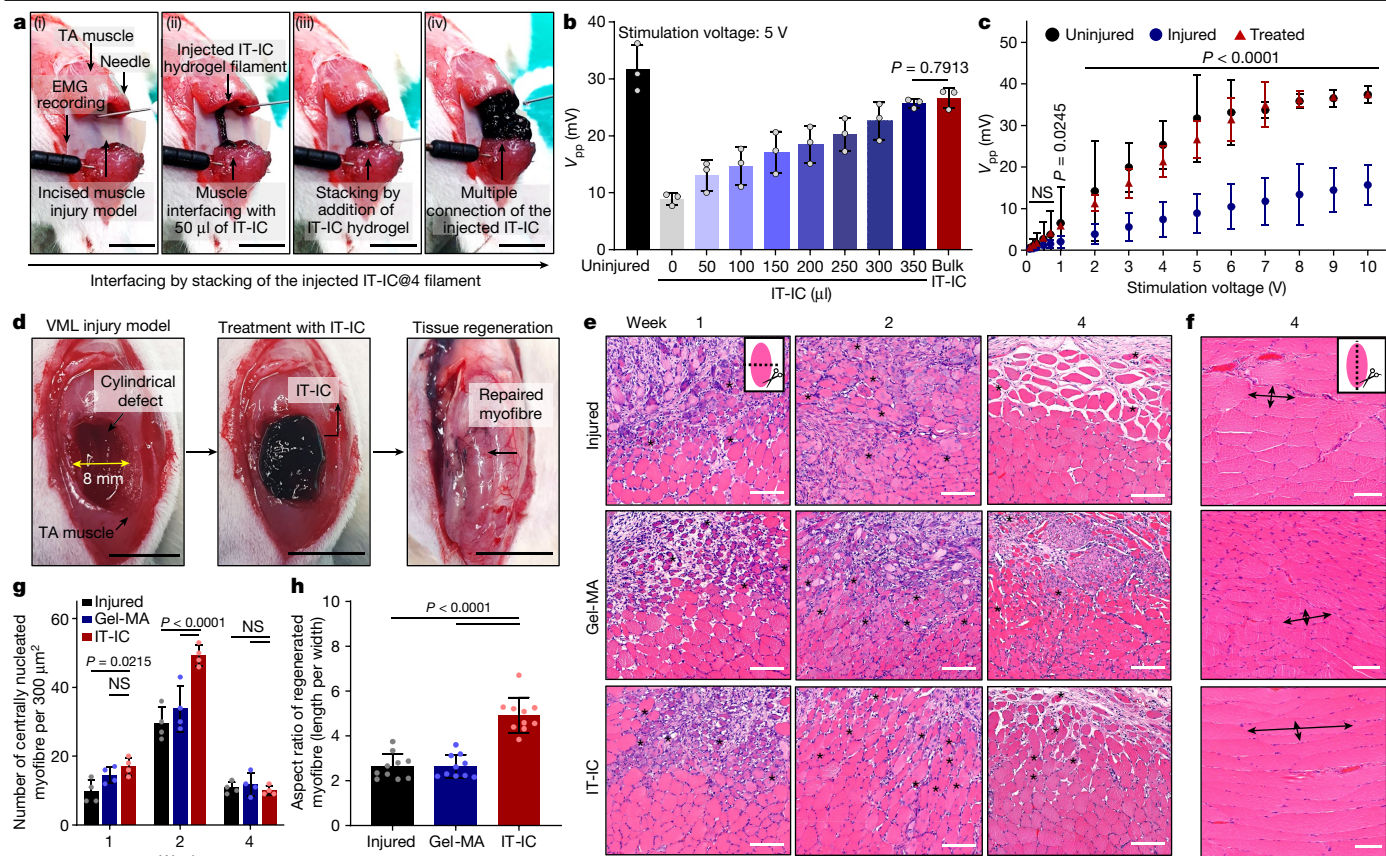


**Fig. 3 | Skeletal muscle-tissue prosthesis through IT-IC hydrogel injection.**

**a**, Experimental procedures for in vivo muscle-tissue conduction of IT-IC@4 in the severe VML model (i). The photos (ii)–(iv) show stacking of each IT-IC@4 filament to fill in the tissue defect. Scale bars, 5 mm. **b**, EMG amplitude evoked by electrical stimulation (mean  $\pm$  s.d.;  $n = 3$  for independent experiments) while filling the defect with the filaments. One-way analysis of variance (ANOVA), Tukey’s post-hoc test, NS (not significant) at  $P = 0.7913$ . **c**, EMG amplitude (mean  $\pm$  s.d.;  $n = 3$  for rats) recorded in uninjured rats and in injured rats either untreated or treated with bulk IT-IC@4.  $P$  values for comparing the injured and treated groups were calculated using two-way ANOVA and Tukey’s post-hoc test. **d**, Photos showing a sequential process from induction of VML injury to

treatment with IT-IC hydrogel and muscle-tissue regeneration at 4 weeks. Scale bars, 1 cm. **e, f**, H&E-stained cross-sectional (**e**, at 1, 2, and 4 weeks) and longitudinal (**f**, 4 weeks) images of the regenerated muscles. Asterisks indicate centrally nucleated myofibres (**e**); arrows indicate their aspect ratios (**f**). Scale bars in **e**, 100  $\mu$ m. **g, h**, Quantitative analysis of the number of centrally nucleated myofibres (**g**) (mean  $\pm$  s.d.;  $n = 4$  for random regions) and their aspect ratios (**h**) (mean  $\pm$  s.d.;  $n = 10$  for random regions). For **e**, two-way ANOVA and Tukey’s post-hoc test,  $P = 0.0215$  for injured versus IT-IC,  $P = 0.5923$  for Gel-MA versus IT-IC (1 week),  $P < 0.0001$  for injured versus IT-IC and Gel-MA versus IT-IC (2 weeks), NS at  $P > 0.05$ . For **f**, one-way ANOVA and Tukey’s post-hoc test,  $P < 0.0001$  for injured versus IT-IC and Gel-MA versus IT-IC (4 weeks).

of inflammatory or immune cells (Supplementary Figs. 23–25 and Supplementary Note 9). In addition, the dissociated AuNPs from IT-IC@4 showed relatively higher accumulation in kidneys, liver and spleen but did not cause significant toxicity (Supplementary Fig. 26 and Supplementary Note 9). In summary, muscle-tissue interfacing by IT-IC hydrogels enables instant tissue–tissue electrical conduction at an early stage after injection as well as further tissue repair at later stages.

### Sensory and motor signalling

Conventional diagnosis and treatment tools have limitations in their use because of the inaccessible tissue surface and insufficient feedback capabilities (details in Supplementary Fig. 27 and Supplementary Note 10). The IT-IC hydrogel can overcome such limitations owing to its stretchability, modulus matching, low impedance and pattern-controllable injectability. Notably, our IT-IC hydrogel showed a much higher tensile adhesion strength of  $8.8 \pm 2.1$  kPa on nerve than other existing materials (methacrylated hyaluronic acid (MeHA),  $1.9 \pm 0.6$  kPa; Gel-MA,  $1.3 \pm 0.6$  kPa; HA–PB,  $0.9 \pm 0.4$  kPa) (Fig. 4a). Owing to its exceptional nerve adhesion, the IT-IC hydrogel injected

on the rat sciatic nerve was stably maintained without delamination issues, even in stretching or bending modes (Fig. 4b). For immediate and safe access to the nerve using conventional electrical wires, IT-IC hydrogels were sequentially injected in the form of small sphere-like structures (Fig. 4c).

These unique features allowed the interface between the nerve and IT-IC hydrogel to facilitate the recording of different sensory neural responses to three modes of mechanical stimulation: strong brushing, weak brushing or tapping of the sole of the rat’s foot (Fig. 4d and Supplementary Figs. 28 and 29). The signal-to-noise ratio (SNR; strong brushing,  $3.0 \pm 0.4$ ; weak brushing,  $1.9 \pm 0.3$ ; tapping,  $0.7 \pm 0.2$ ) values corresponding to the individual events are almost identical to the SNRs of sensory neural signals previously reported<sup>33</sup> (Fig. 4e). In addition to the mechanoreceptor-to-nerve pathway, the connection was tested in reverse, and stimulation of the nerve with varying frequencies (5, 10, 20 and 50 Hz) and amplitudes (0.1–0.9 V) effectively induced hind-limb muscle contractions without any tissue damage (Fig. 4f–i, Supplementary Fig. 30 and Supplementary Videos 2 and 3). The trend of ankle contraction after the applied voltages matched the EMG signals, indicating that the nerve-to-muscle signalling pathway can be precisely controlled by the IT-IC hydrogel.

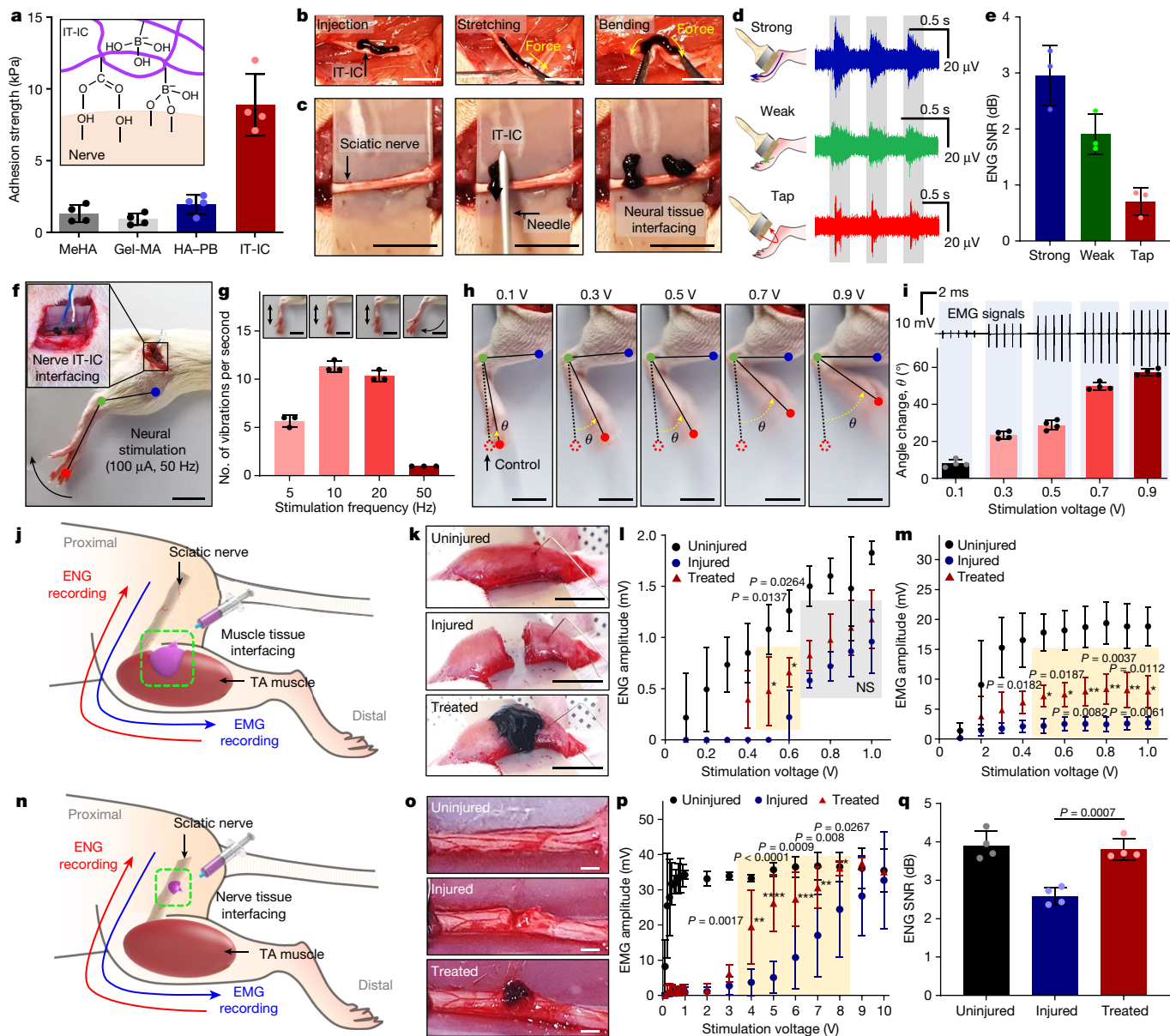


**Fig. 4 | Bidirectional sensory and motor signalling of IT-IC hydrogels in the neuromuscular system.** **a**, Nerve adhesion strength of the IT-IC hydrogel (mean  $\pm$  s.d.;  $n = 4$  for samples). The inset shows its mechanism of adhesion to the nerve. **b**, Photographs showing the deformability during stretching and bending of hydrogels injected on the nerve. Scale bars, 5 mm. **c**, Images of injected hydrogels interfacing with nerves. Scale bars, 1 cm. **d, e**, Sensory signalling under three different mechanical stimulations (strong or weak brushing and tapping) (**d**) and its SNRs (**e**) (mean  $\pm$  s.d.;  $n = 3$  for stimulation). **f**, A photograph of electrical neural stimulation through IT-IC hydrogel interfacing (inset). **g**, Plot of the number of leg vibrations per second against stimulation frequency (mean  $\pm$  s.d.;  $n = 3$  for stimulation). Insets correspond to sequential leg responses to stimulations. **h, i**, Photographs of ankle changes resulting from the applied voltages (**h**) and the degree of ankle movement

under each voltage stimulation (**i**) (mean  $\pm$  s.d.;  $n = 4$  for stimulation). **j–m**, Bidirectional signalling in uninjured, injured and IT-IC-treated muscles. Overall scheme (**j**) and experimental photos (**k**) are shown for each group. **l, m**, ENG (**l**, mean  $\pm$  s.d.;  $n = 4$  for rats) and EMG (**m**, mean  $\pm$  s.d.;  $n = 5$  for rats) amplitudes for each group induced by voltage stimulation to the muscle (**l**) or nerve (**m**). Scale bars in **f, g, h** and **k, l**. **n–q**, Bidirectional signalling in uninjured, injured and IT-IC-treated nerves. Overall scheme (**n**) and experimental photos (**o**) are shown for each group. Scale bars in **o**, 2 mm. **p**, EMG amplitudes (mean  $\pm$  s.d.;  $n = 3$  for rats) monitored in each group under voltage stimulations on the nerve. **q**, SNRs of ENG signals recorded under mechanical stimulation (mean  $\pm$  s.d.;  $n = 4$  for stimulation). Two-way ANOVA (**l, m**, and **p**) or one-way ANOVA (**q**) followed by Tukey's post-hoc test  $P$  values for comparisons with the injured group.

To better investigate the feasibility of our bidirectional sensory and motor signalling for C-RAR, we first confirmed the electroneurogram (ENG) recording performance (Fig. 4j, red arrow) of the IT-IC hydrogel when uninjured, injured and IT-IC hydrogel-treated muscles were electrically stimulated with an increase in the applied voltages (0–1 V) (Fig. 4j–l). ENG signals were detected at 0.4 V for the IT-IC hydrogel-treated case, whereas the ENG signals in the injured condition were detected at 0.6 V (Fig. 4l). Although the ENG signal amplitudes in the

uninjured case (for example,  $1.08 \pm 0.24$  mV at 0.5 V) were slightly higher than those in the treated case (for example,  $0.48 \pm 0.33$  mV at 0.5 V), the IT-IC hydrogel was clearly effective in providing both muscle-bridging and nerve-signal-monitoring capabilities. Conversely, EMG measurements (blue arrow) were recorded under the same three conditions while applying voltages (0–1 V) to the peripheral nerve (Fig. 4m). As expected, the IT-IC hydrogel also efficiently interfaced with the corresponding nerve and muscle tissues, resulting in higher EMG

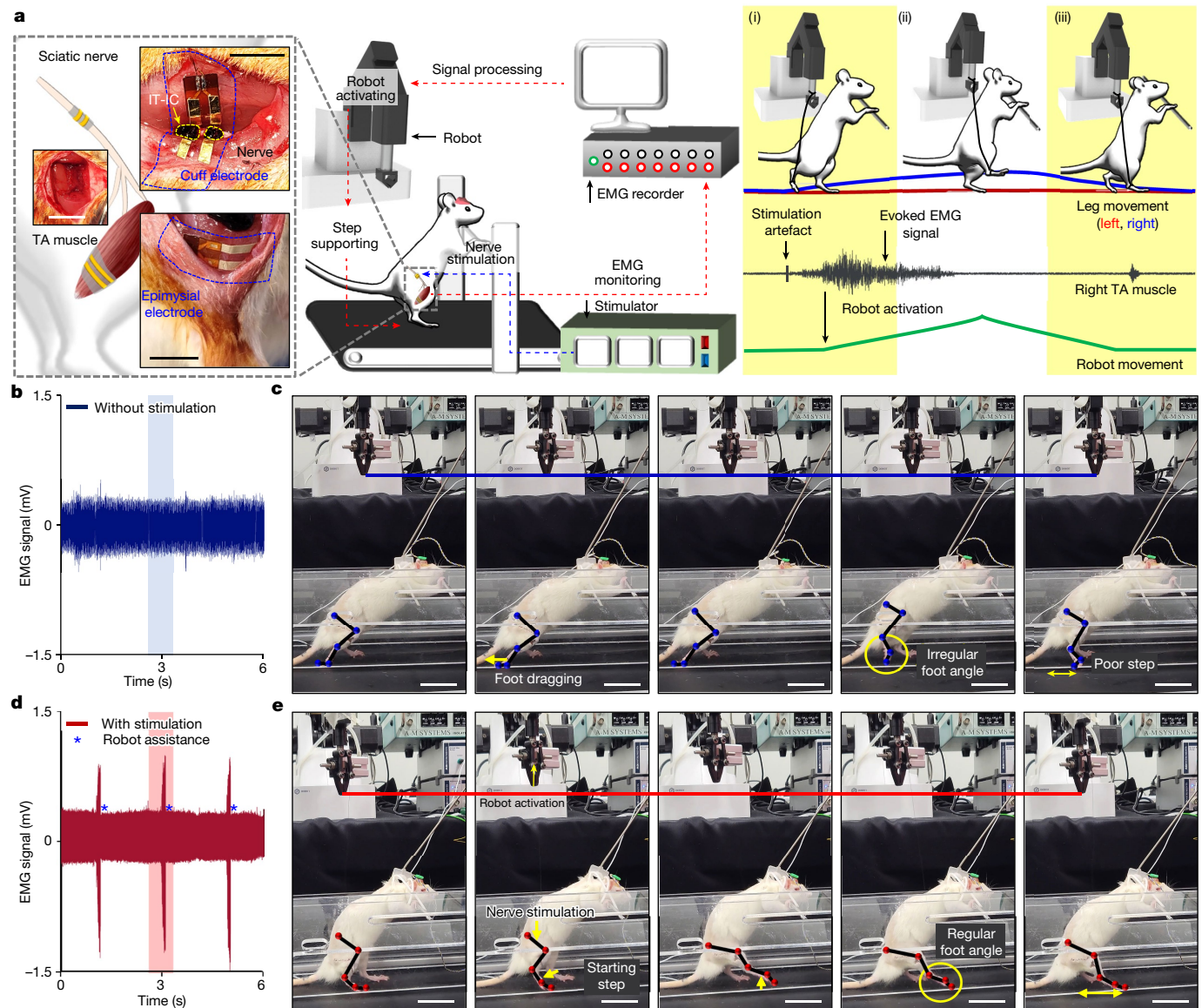


**Fig. 5 | C-RAR system using IT-IC hydrogel.** **a**, Schematic illustration showing the sequential operation of the C-RAR system comprising IT-IC hydrogels, a robot, a treadmill and self-healing stretchable cuff and epimysial electrodes. The C-RAR system can lift the rat’s injured right hind limb through precise monitoring of EMG signals and feedback-controlled electrical nerve stimulation. Scale bars, 1 cm. **b**, EMG signals from the awake rat 3 days after surgery with VML injury without application of electrical stimulation to the sciatic nerve.

**c**, Photographs showing gait failure (foot dragging, irregular foot angles and poor steps) of the injured rat in the absence of robot assistance. **d**, EMG signal measurement from the awake rat 3 days after surgery with VML injury when electrical stimulation is applied to the sciatic nerve using the cuff electrode. **e**, Photographs showing that nerve stimulation triggers instantaneous robot assistance, enabling the injured rat to walk with a normal gait and regular foot angles. Scale bars in **c** and **e**, 5 cm.

signal amplitudes (for example,  $31.45 \pm 2.66$  mV at 0.5 V) than for the injured case (for example,  $0.68 \pm 1.18$  mV at 0.5 V). In addition to IT-IC hydrogel interfacing in the muscle defect model, our bidirectional functionality was demonstrated on the notched nerve and uninjured muscle tissues (Fig. 4n,o). It was noted that IT-IC hydrogel treatment resulted in more effectively delivery of sensory and motor signals compared with the injured case (Fig. 4p, EMG monitoring under nerve stimulation; Fig. 4q, SNR comparison of recorded ENG under mechanical stimulation). In other words, the EMG signal amplitude shown in the treated case ( $26.21 \pm 8.02$  mV at 5 V) was higher than in the injured case ( $5.07 \pm 1.96$  mV at 5 V). Similarly, the ENG signal amplitude shown in the treated case ( $3.81 \pm 0.28$  dB at mechanical stimulation of 1.2 N) was higher than in the injured case ( $2.59 \pm 0.23$  dB at mechanical stimulation of 1.2 N). In addition, no biological safety issues of IT-IC@4 on the nerve were detected (Supplementary Fig. 31 and Supplementary Note 11).

### Closed-loop rehabilitation

In line with our continuous efforts to develop the IT-IC hydrogel with effective charge delivery and tissue regeneration capabilities and apply it to in vivo bidirectional sensory and motor signalling in anaesthetized rats (Supplementary Figs. 32 and 33 and Supplementary Video 4), we further applied the IT-IC hydrogel to C-RAR, for which awakened rats with muscle injury could move around at an early stage (Fig. 5). To prepare for establishing the C-RAR system, a self-healing and stretchable cuff electrode was first wrapped around the rat’s sciatic nerve coated with the IT-IC hydrogel to deliver electrical stimulation (Fig. 5a, top and right inset showing the corresponding image; Supplementary Fig. 34). To measure the EMG evoked by the aforementioned nerve stimulation and then transmitted to the robot motion-triggering system, a stretchable electrode was also implanted into the epimysium

coated with the IT-IC hydrogel (Fig. 5a, bottom and right inset showing the corresponding image; Supplementary Fig. 35). On the basis of such a setup, the robot is intended to aid the rat's gait while it walks on the treadmill. Thus, the robot assistance was programmed so that its motion was activated to lift the rat's foot when the average of the EMG signals within 50 ms recorded from the epimysial electrode implanted into the right tibial anterior muscle exceeded a threshold (Fig. 5a, right; schematics of the C-RAR system and sequential steps of (i) detection of nerve stimulation-evoked EMG signal, (ii) robot-assisted gate of the rat's right leg and (iii) return of the robot to standby status when the right leg swing is temporarily stopped; Supplementary Figs. 36–38). The activated C-RAR system triggers feedback stimulation that can be changed in proportion to the degree of changes in the averaged EMG signal without undesired open-loop divergence (Supplementary Fig. 39 and Supplementary Note 12).

To demonstrate the C-RAR system for immediate movement recovery of an awake rat 3 days after surgery with VML injury, we used the bidirectional nerve- and muscle-interfacing function (Fig. 5b–e, Supplementary Fig. 40 and Supplementary Video 5). In a control condition (without nerve stimulation), the spontaneous contraction of injured muscle tissues could generate only small tibialis anterior (TA) EMG signals that were rarely above the threshold voltage, leading to gait failure (foot dragging, irregular foot angles and poor steps) without the aid of robot assistance (Fig. 5c and Supplementary Fig. 40). However, when the nerve stimulation was applied to the rat's right leg, compound EMG signals were evoked followed by clear detection over the threshold voltage (Fig. 5d), thus successfully triggering robot assistance to fully support the rat's normal gait with regular foot angles (Fig. 5e and Supplementary Fig. 40). To better show the instantaneous robot-assisted rehabilitation (RAR) performance, we prepared a control experiment in which the IT-IC hydrogel and peripheral nerve interface (PNI)-based nerve stimulation were not applied to the injured rat (see Methods, Extended Data Fig. 1, Supplementary Video 6 and Supplementary Fig. 41 for details of gait of each group). Under these conditions, the absence of the muscle–hydrogel interface prevented the instantaneous robot assistance from functioning. Notably, when IT-IC hydrogel was applied to the injured muscle tissue, the resulting conduction allowed the RAR system to function immediately. Although the RAR system alone, without PNI-based nerve stimulation, showed reliable closed-loop results, such a function is limited to muscle tissues with moderate injuries. In this regard, our C-RAR system can be a promising candidate for efficient robot-enabled rehabilitation.

## Conclusion

Injectable prostheses consisting of soft and conductive hyaluronic hydrogels lead to instantaneous C-RAR through muscle and peripheral nerve tissue conduction in the early stage after injury and enhancement of tissue repair in the later stage. In the hydrogel network, dynamic coordinate bonds aided by rearrangeable biphenyl bonds play a critical role in securing a desirable mechanical modulus similar to that of tissue, great injectability by efficient energy dissipation against shear stress, conformal contact on rough-tissue interfaces and strain-resistant electrical conductivity. Applying IT-IC hydrogels to tissue defects and device–tissue interfaces implements transmission and monitoring of electrophysiological signals. Ultimately, the injectable prosthesis platform brings bidirectional crosstalk between muscle and peripheral nerve tissues for therapeutic recovery in patients with chronic tissue injury.

## Online content

Any methods, additional references, Nature Portfolio reporting summaries, source data, extended data, supplementary information, acknowledgements, peer review information, details of author contributions

and competing interests, and statements of data and code availability are available at <https://doi.org/10.1038/s41586-023-06628-x>.

- Jiang, Y. et al. Wireless, closed-loop, smart bandage with integrated sensors and stimulators for advanced wound care and accelerated healing. *Nat. Biotechnol.* **41**, 652–662 (2022).
- Mickle, A. D. et al. A wireless closed-loop system for optogenetic peripheral neuromodulation. *Nature* **565**, 361–365 (2019).
- Won, S. M., Song, E., Reeder, J. T. & Rogers, J. A. Emerging modalities and implantable technologies for neuromodulation. *Cell* **181**, 115–135 (2020).
- Yuk, H., Lu, B. & Zhao, X. Hydrogel bioelectronics. *Chem. Soc. Rev.* **48**, 1642–1667 (2019).
- Deng, J. et al. Electrical bioadhesive interface for bioelectronics. *Nat. Mater.* **20**, 229–236 (2021).
- Boys, A. J. et al. 3D bioelectronics with a remodelable matrix for long-term tissue integration and recording. *Adv. Mater.* **35**, 2207847 (2022).
- Strakosas, X. et al. Biostack: nontoxic metabolite detection from live tissue. *Adv. Sci.* **9**, 2101711 (2022).
- Lim, C. et al. Tissue-like skin-device interface for wearable bioelectronics by using ultrasoft, mass-permeable, and low-impedance hydrogels. *Sci. Adv.* **7**, eabd3716 (2021).
- Lacour, S. P., Courtine, G. & Guck, J. Materials and technologies for soft implantable neuroprostheses. *Nat. Rev. Mater.* **1**, 16063 (2016).
- Squair, J. W. et al. Neuroprosthetic baroreflex controls haemodynamics after spinal cord injury. *Nature* **590**, 308–314 (2021).
- Yang, Q. et al. Photocurable bioresorbable adhesives as functional interfaces between flexible bioelectronic devices and soft biological tissues. *Nat. Mater.* **20**, 1559–1570 (2021).
- Liu, Y. et al. Soft and elastic hydrogel-based microelectronics for localized low-voltage neuromodulation. *Nat. Biomed. Eng.* **3**, 58–68 (2019).
- Wang, L. et al. Injectable and conductive cardiac patches repair infarcted myocardium in rats and minipigs. *Nat. Biomed. Eng.* **5**, 1157–1173 (2021).
- Zhou, L. et al. Soft conducting polymer hydrogels cross-linked and doped by tannic acid for spinal cord injury repair. *ACS Nano* **12**, 10957–10967 (2018).
- Liang, S. et al. Paintable and rapidly bondable conductive hydrogels as therapeutic cardiac patches. *Adv. Mater.* **30**, 1704235 (2018).
- Trevathan, J. K. et al. An injectable neural stimulation electrode made from an in-body curing polymer/metal composite. *Adv. Healthcare Mater.* **8**, 1900892 (2019).
- Yu, Q., Jin, S., Wang, S., Xiao, H. & Zhao, Y. Injectable, adhesive, self-healing and conductive hydrogels based on MXene nanosheets for spinal cord injury repair. *Chem. Eng. J.* **452**, 139252 (2023).
- Zhao, X., Guo, B., Wu, H., Liang, Y. & Ma, P. X. Injectable antibacterial conductive nanocomposite cryogels with rapid shape recovery for noncompressible hemorrhage and wound healing. *Nat. Commun.* **9**, 2784 (2018).
- Sun, J.-Y. et al. Highly stretchable and tough hydrogels. *Nature* **489**, 133–136 (2012).
- Guan, Y. & Zhang, Y. Boronic acid-containing hydrogels: synthesis and their applications. *Chem. Soc. Rev.* **42**, 8106–8121 (2013).
- Golestanzadeh, M. & Naeimi, H. Palladium decorated on a new dendritic complex with nitrogen ligation grafted to graphene oxide: fabrication, characterization, and catalytic application. *RSC Adv.* **9**, 27560–27573 (2019).
- Liu, C.-H. et al. Metal oxide-containing SBA-15-supported gold catalysts for base-free aerobic homocoupling of phenylboronic acid in water. *J. Catal.* **336**, 49–57 (2016).
- Guimarães, C. F., Gasperini, L., Marques, A. P. & Reis, R. L. The stiffness of living tissues and its implications for tissue engineering. *Nat. Rev. Mater.* **5**, 351–370 (2020).
- Han, I. K. et al. Electroconductive, adhesive, non-swelling, and viscoelastic hydrogels for bioelectronics. *Adv. Mater.* **35**, 2203431 (2023).
- Martin-Drumel, M. et al. Low-energy vibrational spectra of flexible diphenyl molecules: biphenyl, diphenylmethane, bibenzyl and 2-, 3- and 4-phenyltoluene. *Phys. Chem. Chem. Phys.* **16**, 22062–22072 (2014).
- Gao, Z., Su, R., Huang, R., Qi, W. & He, Z. Glucosaminan-mediated facile synthesis of gold nanoparticles for catalytic reduction of 4-nitrophenol. *Nanoscale Res. Lett.* **9**, 1–8 (2014).
- Schoenmakers, D. C., Rowan, A. E. & Kouwer, P. H. Crosslinking of fibrous hydrogels. *Nat. Commun.* **9**, 2172 (2018).
- Dawn, A. et al. Investigating the effect of supramolecular gel phase crystallization on gel nucleation. *Soft Matter* **14**, 9489–9497 (2018).
- Urciuolo, A. et al. Intravital three-dimensional bioprinting. *Nat. Biomed. Eng.* **4**, 901–915 (2020).
- Aurora, A., Garg, K., Corona, B. T. & Walters, T. J. Physical rehabilitation improves muscle function following volumetric muscle loss injury. *BMC Sports Sci. Med. Rehabilitation* **6**, 1–10 (2014).
- Jin, Y. et al. Functional skeletal muscle regeneration with thermally drawn porous fibers and reprogrammed muscle progenitors for volumetric muscle injury. *Adv. Mater.* **33**, 2007946 (2021).
- Zhou, L. et al. Injectable muscle-adhesive antioxidant conductive photothermal bioactive nanomatrix for efficiently promoting full-thickness skeletal muscle regeneration. *Bioact. Mater.* **6**, 1605–1617 (2021).
- Song, K.-I. et al. Adaptive self-healing electronic epineurium for chronic bidirectional neural interfaces. *Nat. Commun.* **11**, 4195 (2020).

**Publisher's note** Springer Nature remains neutral with regard to jurisdictional claims in published maps and institutional affiliations.

Springer Nature or its licensor (e.g. a society or other partner) holds exclusive rights to this article under a publishing agreement with the author(s) or other rightsholder(s); author self-archiving of the accepted manuscript version of this article is solely governed by the terms of such publishing agreement and applicable law.

© The Author(s), under exclusive licence to Springer Nature Limited 2023

## Methods

### Materials

The materials 4-aminophenylboronic acid hydrochloride, *N*-hydroxysuccinimide (NHS), 1-(3-dimethylaminopropyl)-3-ethylcarbodiimide hydrochloride (EDC), gold(III) chloride trihydrate and deuterium oxide were purchased from Sigma-Aldrich and used as received. Sodium hyaluronate (HA; 151–300 kDa) was purchased from Lifecore Biomedical.

### Synthesis of HA–PB

To synthesize HA–PB, 100 mg HA was dissolved in 15 ml of distilled water in a 20 ml vial, and the pH was adjusted to 5.5 by adding 1 mol l<sup>-1</sup> NaOH. EDC (95.85 mg) and NHS (57.55 mg) were added to the HA solution. Then, 4-aminophenylboronic acid (86.7 mg) was added slowly to the HA–EDC–NHS solution (pH 5.5). The mixture was stirred for 24 h, dialysed against distilled water with sodium chloride (9 g l<sup>-1</sup>) for 3 days using a regenerated cellulose dialysis membrane (molecular weight cutoff) and lyophilized for 4 days. The degree of conjugation of boronic acid was determined by proton-nuclear magnetic resonance (<sup>1</sup>H NMR, Oxford 300 NMR, VARIAN) spectroscopy, and the integration value was calculated with MestReNova v.6.0.2. For that, the lyophilized HA–PB (7.5 mg) was dissolved in deuterium oxide (750 μl).

### Fabrication of IT-IC hydrogels

To prepare the IT-IC hydrogel, the HA–PB<sub>low</sub> or HA–PB<sub>high</sub> was dissolved in distilled water at a final concentration of 2 wt%. Then, NaOH (concentration of stock solution = 1 mol l<sup>-1</sup>; half the volume was treated first, and the remainder treated after adding HAuCl<sub>4</sub>) and HAuCl<sub>4</sub> (100 mmol l<sup>-1</sup>) were sequentially added to the HA–PB solution (a total volume of 400 μl) at various ratios (NaOH/Au<sup>3+</sup> ratio = 1, 2, 4 or 6). The reaction proceeded for at least 120 min. Furthermore, the HA–PB<sub>high</sub> hydrogels with 1 and 3 wt% were prepared at a NaOH/Au<sup>3+</sup> ratio of 4 in the same manner. To prepare the less-conductive IT-IC hydrogel, HA–PB<sub>high</sub> hydrogels with 5 and 10 μl of HAuCl<sub>4</sub> were prepared at a NaOH/Au<sup>3+</sup> ratio of 4 in the same manner.

### Rheological analysis

The storage (*G'*) and loss (*G''*) moduli of the IT-IC hydrogels were measured using an HR10 rheometer (TA Instruments) under oscillatory frequency sweep mode (0.1–10 Hz, at 1% strain) with a 20 mm plate geometry and gap size of 100 μm at room temperature. In addition, the shear viscosity of IT-IC@4 was monitored as the shear rate increased from 0.01 to 100 s<sup>-1</sup>. To demonstrate self-healing properties, the *G'* and *G''* values of the IT-IC hydrogels were measured under alternating strains of 1% and 1,000% at a fixed frequency of 1 Hz. Each strain was applied to the hydrogels for 180 s. To investigate the gelation time, the *G'* and *G''* moduli of either IT-IC@2 or IT-IC@4 (at 1 Hz, 1% of strain) were measured as a function of time after mixing the polymer, NaOH and Au<sup>3+</sup>.

### Chemical characterization of IT-IC hydrogels

To investigate the gelation mechanism of the IT-IC hydrogels, XPS and FT-IR analyses were conducted. First, for XPS analysis (Thermo ESCALAB250), samples prepared with two NaOH/Au<sup>3+</sup> ratios (1 or 4) and HA–PB dissolved in distilled water (2 wt%) were dried onto a silicon wafer. The obtained raw spectra of each sample were deconvoluted using Origin 5 software. Second, for FT-IR analysis (ATR FT-IR; IFS 66 v/S, Bruker), the sample was prepared in the same manner as for XPS, and the spectrum was obtained in the wavenumber ranging from 4,000 to 600 cm<sup>-1</sup>.

### Size analysis of AuNPs in the IT-IC hydrogels

The size of AuNPs distributed in the IT-IC hydrogels was analysed in two ways: ultraviolet–visible (UV-vis) spectroscopy (Agilent 8453) and transmission electron microscopy (TEM) (JEM–2100F, JEOL).

For sample preparation, 100 μl of IT-IC hydrogel was vigorously vortexed, dispersed in 900 μl of distilled water and centrifuged. The absorption spectra of the supernatant solution were analysed using the UV–vis detector, and part of the solution (5 μl) was drop-cast in 300-mesh copper grids and dried for TEM. In the TEM images, the size of the AuNPs was measured with ImageJ software.

### Conformal contact test of the IT-IC hydrogels

To evaluate the conformal contact ability of the IT-IC hydrogels, freshly dissected TA muscle tissues (Sprague Dawley (SD) rat, male, 300–350 g, 10 weeks) and 3D curved objects were prepared. IT-IC@4 encapsulating fluorescein isothiocyanate (Sigma-Aldrich) was applied to muscle tissue stained with rhodamine B (Sigma-Aldrich). A cross-sectional fluorescent image was obtained by confocal microscope (Leica TCS SP8 STED). Furthermore, the conformability on the curved objects was evaluated using injected filaments (26 and 18G). A mould with various curvature from 0.1 to 0.9 (the difference of each hill and valley was 0.05) was fabricated by stereolithography apparatus (SLA) type 3D printing (commissioned by a company, 3D PRO). The optical images were obtained by simple magnifier (PS-EM307, Presentshop).

### Computational MD simulations

The hydrogel system was constructed using two polymeric backbone chains crosslinked with biphenyl rings at a ratio of ten monomer units to one biphenyl group. To incorporate water into the system, the extended simple point charge (SPC/E) water model<sup>34</sup> was used, being filled to 80% of the total weight. LigParGen force-field mapping<sup>35</sup> was used to represent the hydrogel at an all-atomic level. To accurately account for long-range electrostatic interactions, the particle–particle mesh solver method was used. The MD calculations were performed with a time step of 2 × 10<sup>-15</sup> s. Before the MD simulation, the FIRE algorithm was used for energy minimization. A 10 ns isothermal–isobaric (NPT) simulation was carried out using the Nosé–Hoover thermostat<sup>36</sup> and the Parrinello–Rahman barostat<sup>37</sup>, maintaining the system at a temperature of 300 K and a pressure of 1.0 bar. Following the NPT simulation, a shear deformation MD simulation was conducted in the *xz* plane, applying a constant shear rate of 10<sup>8</sup> per second, until a strain (=  $dx/z$ ) of 2 was reached. For the entire simulation process, the LAMMPS software package<sup>38</sup> was used as the computational tool.

### Electrical characterization of the IT-IC hydrogels

To investigate the electrical resistance of IT-IC hydrogels, samples were prepared with a cylindrical shape (diameter, length: 4.78 mm, 20 mm) of bulk IT-IC hydrogel and filaments were extruded with different gauges of needle (diameter, length: 0.63 mm, 20 mm (26G); 2.29 mm, 20 mm (23G); 3.53 mm, 20 mm (18G)). The electrical resistance ( $\Omega$ ) was measured using a four-point probe method (Keithley 2450 source meter; Keithley) with equal probe spacing of 5 mm. From the resistance of bulk hydrogel, the conductivity at 0% strain was calculated using the following equation:

$$\text{Conductivity (S cm}^{-1}\text{)} = l/(A \times R)$$

where *A* is the cross-sectional area of the hydrogel (cm<sup>2</sup>), *l* is the length of hydrogel (cm) and *R* is the measured resistance ( $\Omega$ ). Using a sample with initial length of 5 mm, the change in resistance was measured while stretching at 1 mm s<sup>-1</sup> (strain ranging from 0 to 100%). Then, the electrical hysteresis of the sample was measured at the same stretching–releasing speed up to various strains (from 0% to 100%).

### Animal experiments

All animal experiments were conducted with approval from the Institutional Animal Care and Use Committee of Sungkyunkwan University (SKKUIACUC2021-03-28-1 and SKKUIACUC2022-08–36-2) and under published standards for humane animal care (*n* = 3 or 5).

In addition, the authors conducted all animal experiments in accordance with the ethical protocol given by the Korean Ministry of Health and Welfare.

### **In vivo muscle-tissue-IT-IC hydrogels interfacing test**

To verify the efficient charge transfer of IT-IC hydrogels at muscle tissue–tissue interfaces, an in vivo muscle defect model was used (SD rats male, 300–350 g, 10 weeks). The TA muscles were first separated on Teflon tape to prevent electrical conduction to other muscles and cut using a scalpel. The cut muscles were spaced approximately 5 mm apart. The upper muscle of the damaged region was electrically stimulated using two pin-shaped single electrodes with a waveform generator (Arbitrary, 1 Channel, 20 MHz, 33511B, Keysight Technologies, Inc.). While IT-IC@4 was injected into the damaged region (total volume = 400  $\mu$ l, injections of 50  $\mu$ l each with a 26G needle), the EMG signals from the bottom muscle were recorded using biosignal amplifiers (Bio Amp FE231, AD instruments) and a data acquisition device (PowerLab 8/35, AD instruments) with cathode and anode electrodes inserted at 2 cm intervals into the bottom of the TA muscle and reference electrodes inserted into the tail. The EMG signals were filtered according to the ISEK (International Society of Electrophysiology and Kinesiology) standard (1,500 Hz, low pass). Furthermore, for evaluation of the EMG recording capability of IT-IC hydrogels, we conducted the aforementioned stimulation, recording and signal processing experiments in normal animals (SD rats, male, 300–350 g, 10 weeks). The IT-IC hydrogel was applied to the rat's TA muscle and two pin-type electrodes for EMG recording were inserted into it. The recorded EMG signals were compared with those recorded from the muscle without hydrogel.

### **Histological analysis**

To evaluate muscle-tissue repair by implantation of IT-IC hydrogel, the VML model (SD rats, male, 300–350 g, 10 weeks) with a 3-mm-deep cylindrical defect (diameter = 8 mm) was used. IT-IC or Gel-MA hydrogel (200  $\mu$ l) was implanted in the defect region. For histological analysis, the rats were killed 1, 2 or 4 weeks later, and the tissue was fixed in 4% (v/v) paraformaldehyde solution. The tissue specimen was sectioned in the cross-sectional or longitudinal direction and stained with haematoxylin and eosin (or Masson-trichrome staining agent for the IT-IC@4 group; American MasterTech Scientific). All procedures were commissioned by GENOSS. At randomly selected positions on the H&E-stained images, the number of centronucleated myofibres and the aspect ratio of the myofibres were measured using ImageJ software. For Masson-trichrome stained images, the fibrotic area (%) was calculated by the following equation. Each area was quantified using ImageJ software.

$$\text{Fibrotic area (\%)} = \frac{\text{blue coloured area}}{\text{total stained (red and blue coloured) area}} \times 100$$

For immunofluorescence staining, the freshly dissected muscle tissue was embedded in Tissue-Tek OCT compound (Sakura) and serially sectioned at 10  $\mu$ m using a cryomicrotome. The tissue slides were incubated in primary antibody solutions as follows: (phycoerythrin (PE)-conjugated CD3e monoclonal (145-2C11) (1:1,000, Invitrogen, USA); FITC-conjugated anti-mouse CD8a (1:1,000, BioLegend); APC-eFluor 780 conjugated CD11b monoclonal (M1/70) (1:1,000, Invitrogen); APC-conjugated F4/80 monoclonal (BM8) (1:1,000, Invitrogen); and anti-laminin (ab11575, 1:400; Abcam)). Alexa-Fluor-488-conjugated goat anti-rabbit IgG (1:400, Invitrogen) was used as secondary antibodies to stain laminin green. Cell nuclei were counterstained with 4',6-diamidino-2-phenylindole (DAPI). The number of positive inflammatory cells was counted in randomly selected immunofluorescence-stained images and calculated per  $\text{mm}^2$ .

### **Adhesiveness of IT-IC hydrogels on nerve tissue**

The adhesive strength of the hydrogels on nerve tissue was measured using a universal testing machine (34SC-1, Instron). The peroneal nerve was dissected from the pig's forelimbs, cut into 1 cm  $\times$  0.5 cm pieces and fixed on a T-shaped holder (surface area, 20  $\times$  20  $\text{mm}^2$ ; height, 20 mm) using conventional Superglue. For control groups, MeHA, Gel-MA hydrogels and HA–PB pre-gel solution were prepared (Supplementary Methods). The HA–PB polymer was dissolved in distilled water at a final concentration of 2 wt%. All samples were spread on the epineurium of one nerve tissue and squeezed with another tissue piece. Tensile stress was applied to the terminal of the holder using a 50 N load cell at a speed of 0.5  $\text{mm s}^{-1}$ . The tensile adhesive strength (kPa) was calculated by dividing the maximum load (N) by the attached area ( $\text{m}^2$ ).

### **The RAR/C-RAR system using IT-IC hydrogels**

IT-IC hydrogel was injected into the surfaces of the TA muscle and sciatic nerve of rats with VML injury. As-prepared intrinsically stretchable electrodes were conformally mounted onto the TA muscle and the sciatic nerve. The stretchable devices used as either cuff-type neural interfacing or epimysial electrodes were wired to external interconnects fixed to the heads of IT-IC hydrogel-treated VML rats (Supplementary Methods). The external interconnects and wire-shaped electrodes penetrating the rat's tail were connected to the waveform generator and data acquisition device, respectively. The sciatic nerve of the rat was electrically stimulated every 3 s with a specific pulse (duration of 1 ms) applied by the waveform generator. This stimulation was applied to rats walking on the treadmill (LT320, LAIYUE BIOTECH) at a speed of 3  $\text{m min}^{-1}$  and was adjusted depending on the level of EMG signals as follows. Considering the electrical stimulation, we set the initial parameters (initial stimulation amplitude of 50 mV, update weights of 5, EMG threshold (multiplying by 15) and window size (5,000 samples every 50 ms)). EMG signals were then recorded in real time at a sampling frequency of 100 kHz. The EMG signals were simultaneously processed with a band-pass filter (200 to 1,500 Hz) to remove noise associated with rat movements. The processed EMG signals were confirmed using LabChart 8 Pro (AD Instruments) software. The absolute values of the signals filtered during 50 ms were calculated in real time to take the mean value using MATLAB software, for which codes were designed using the Labchart-MATLAB application programming interface (<https://www.adinstruments.com/support/knowledge-base/can-data-be-streamed-labchart-windows-matlab-while-sampling>) and MATLAB-Dobot Studio application programming interface (<https://www.dobot-robots.com/products/education/magician.html>). We increased the amplitude of the electrical stimulation by 10 mV increments when the averaged EMG signals were lower than the predetermined threshold voltage. If the averaged EMG signals exceeded the threshold value, the cue to trigger the robot (Dobot Magician, DOBOT) assistance at 2 cm in the z axis was activated, and the stimulation amplitude was changed in proportion to the degree of changes in the average EMG signal.

In the RAR system based on muscle–IT-IC interfacing without PNI, the underlying closed-loop operation entailing the electrical stimulation and signal recording processes is almost identical to that of the C-RAR system using muscle– and nerve–IT-IC interfacing. The only difference in this system is that the closed-loop operation is performed on the real-time monitoring and analysis of EMG signals generated from the injured and IT-IC-treated muscle tissues. For quantitative analysis, we manually analysed gait cycle (%) in stance and swing phase modes, maximum toe height and step width data from recorded videos. All videos were analysed with Adobe premiere pro v.22.5, PotPlayer v.1.7.21831 and VapMix2.

### **Statistical analysis**

Statistical analysis was performed using one-way or two-way ANOVA followed by Tukey's post-hoc test using GraphPad Software (Prism v.7).

# Article

*P* values were used to determine significant differences (\**P* < 0.05, \*\**P* < 0.01, \*\*\**P* < 0.001, and \*\*\*\**P* < 0.0001).

## Reporting summary

Further information on research design is available in the Nature Portfolio Reporting Summary linked to this article.

## Data availability

The datasets generated during and/or analysed during the current study are available from the corresponding author upon reasonable request. Source data are provided with this paper.

## Code availability

All customized MATLAB code used for in vivo demonstration in this work is available in a repository at <https://github.com/chwchw2/C-RAR-demo.git>.

34. Berendsen, H. J., Grigera, J. R. & Straatsma, T. P. The missing term in effective pair potentials. *J. Phys. Chem.* **91**, 6269–6271 (1987).
35. Dodda, L. S. et al. LigParGen web server: an automatic OPLS-AA parameter generator for organic ligands. *Nucleic Acids Res.* **45**, W331–W336 (2017).
36. Evans, D. J. & Holian, B. L. The Nose–Hoover thermostat. *J. Chem. Phys.* **83**, 4069–4074 (1985).
37. Parrinello, M. & Rahman, A. Polymorphic transitions in single crystals: a new molecular dynamics method. *J. Appl. Phys.* **52**, 7182–7190 (1981).
38. Plimpton, S. Fast parallel algorithms for short-range molecular dynamics. *J. Comput. Phys.* **117**, 1–19 (1995).

**Acknowledgements** This study was financially supported by the National Research Foundation of Korea grant funded by the Korean government (MSIT) (nos. RS-2023-00208262 (M.S.) and 2020R1C1C1005567 (D.S.)). This research was also supported by the Institute for Basic Science (no. IBS-R015-D1). This research was also supported by the Korean Fund for Regenerative Medicine grant funded by the Korea government (the Ministry of Science and ICT, the Ministry of Health & Welfare) (23B0102L1).

**Author contributions** S.J. conducted experiments for synthesis of the polymers and their characterization. S.J. and H.C. performed all in vivo experiments. D.S. and H.C. conducted electrochemical characterization of the materials. C.-L.Y. and J.-S.K. performed histological analysis and discussed the results. S.R. and W.B.L. conducted computational MD simulations. S.J., H.C., D.S. and M.S. wrote the first draft of the manuscript. M.S. and D.S. conceived and supervised the project. All authors discussed and commented on the data.

**Competing interests** The authors declare no competing interests.

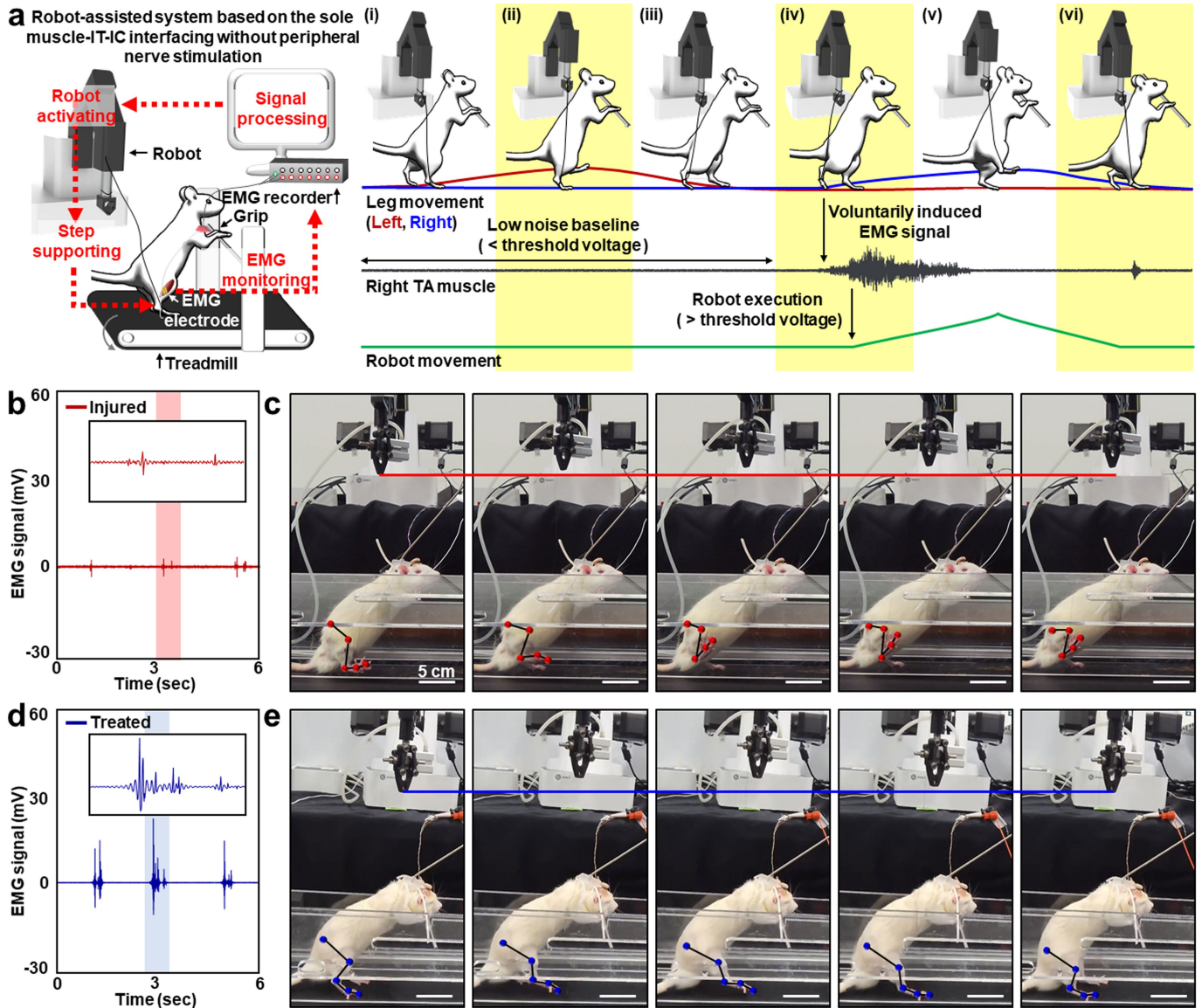
## Additional information

**Supplementary information** The online version contains supplementary material available at <https://doi.org/10.1038/s41586-023-06628-x>.

**Correspondence and requests for materials** should be addressed to Donghee Son or Mikyung Shin.

**Peer review information** *Nature* thanks Milica Radisic and the other, anonymous, reviewer(s) for their contribution to the peer review of this work.

**Reprints and permissions information** is available at <http://www.nature.com/reprints>.



**Extended Data Fig. 1 | The RAR system based on muscle IT-IC interfacing without the sciatic nerve stimulation.** **a**, Schematics of the RAR system based on the TA muscle-tissue conduction by the IT-IC hydrogel without using the peripheral nerve interface. The TA muscle EMG signal evoked by voluntary walking is recorded by the EMG electrode. When specific TA muscle EMG signals are detected, the robotic assistance is activated. The rat's leg movement is then

fully supported by the robotic assistance. **b**, Recorded EMG signals and waveforms (inset) of untreated rats using the RAR system. **c**, Photographs of unsynchronized robot activation and the corresponding abnormal steps. **d**, Recorded EMG signals and waveforms (inset) of IT-IC hydrogel-treated rats using RAR. **e**, Photographs of robotic assistance and the corresponding normal steps.

## Reporting Summary

Nature Portfolio wishes to improve the reproducibility of the work that we publish. This form provides structure for consistency and transparency in reporting. For further information on Nature Portfolio policies, see our [Editorial Policies](#) and the [Editorial Policy Checklist](#).

### Statistics

For all statistical analyses, confirm that the following items are present in the figure legend, table legend, main text, or Methods section.

n/a Confirmed

- The exact sample size ( $n$ ) for each experimental group/condition, given as a discrete number and unit of measurement
- A statement on whether measurements were taken from distinct samples or whether the same sample was measured repeatedly
- The statistical test(s) used AND whether they are one- or two-sided  
*Only common tests should be described solely by name; describe more complex techniques in the Methods section.*
- A description of all covariates tested
- A description of any assumptions or corrections, such as tests of normality and adjustment for multiple comparisons
- A full description of the statistical parameters including central tendency (e.g. means) or other basic estimates (e.g. regression coefficient) AND variation (e.g. standard deviation) or associated estimates of uncertainty (e.g. confidence intervals)
- For null hypothesis testing, the test statistic (e.g.  $F$ ,  $t$ ,  $r$ ) with confidence intervals, effect sizes, degrees of freedom and  $P$  value noted  
*Give  $P$  values as exact values whenever suitable.*
- For Bayesian analysis, information on the choice of priors and Markov chain Monte Carlo settings
- For hierarchical and complex designs, identification of the appropriate level for tests and full reporting of outcomes
- Estimates of effect sizes (e.g. Cohen's  $d$ , Pearson's  $r$ ), indicating how they were calculated

*Our web collection on [statistics for biologists](#) contains articles on many of the points above.*

### Software and code

Policy information about [availability of computer code](#)

Data collection

Bluehill universal was used to obtain adhesive strength and cyclic compression analysis. TRIOS was used to obtain rheology data. Keithley software, Keysight, and ZIVE smart manager software were utilized for the electrical characterization. LabChart 8 Pro and LabVIEW software were used to collect in vivo experimental data. LAS X software and BioTek, Gen 5 data analysis software were used to obtain fluorescence images.

Data analysis

Origin Pro 5, GraphPad Prism 7, and Matlab R2021b were used to analyze and/or plot the data. MestReNova was used to analyze and plot the NMR data. SASView was used to analyze and fit the SAXS data. ImageJ was used to quantify the number of live/dead cells, centronucleated myofibers, fibrosis area, and the number of positive inflammatory cells. Adobe illustrator 26.3.1, Rhinoceros 5, and Keyshot 11 were used to make the illustrations. Chemdraw Ultra 12.0 were used for presenting chemical structures. Adobe premiere pro 22.5, PotPlayer v1.7.21831, and VapMix2 were used to analyze videos frame by frame and to edit supplementary videos.

For manuscripts utilizing custom algorithms or software that are central to the research but not yet described in published literature, software must be made available to editors and reviewers. We strongly encourage code deposition in a community repository (e.g. GitHub). See the Nature Portfolio [guidelines for submitting code & software](#) for further information.

## Data

Policy information about [availability of data](#)

All manuscripts must include a [data availability statement](#). This statement should provide the following information, where applicable:

- Accession codes, unique identifiers, or web links for publicly available datasets
- A description of any restrictions on data availability
- For clinical datasets or third party data, please ensure that the statement adheres to our [policy](#)

The data sets generated during and/or analysed during the current study are available from the corresponding author upon reasonable request.

## Research involving human participants, their data, or biological material

Policy information about studies with [human participants or human data](#). See also policy information about [sex, gender \(identity/presentation\), and sexual orientation](#) and [race, ethnicity and racism](#).

Reporting on sex and gender	N/A
Reporting on race, ethnicity, or other socially relevant groupings	N/A
Population characteristics	N/A
Recruitment	N/A
Ethics oversight	N/A

Note that full information on the approval of the study protocol must also be provided in the manuscript.

## Field-specific reporting

Please select the one below that is the best fit for your research. If you are not sure, read the appropriate sections before making your selection.

- Life sciences       Behavioural & social sciences       Ecological, evolutionary & environmental sciences

For a reference copy of the document with all sections, see [nature.com/documents/nr-reporting-summary-flat.pdf](https://www.nature.com/documents/nr-reporting-summary-flat.pdf)

## Life sciences study design

All studies must disclose on these points even when the disclosure is negative.

Sample size	There are no statistical methods were used to predetermine sample sizes. A minimum of 3 independent experiments were carried out for all in vitro and in vivo studies. To investigate bio distribution profile of gold nanoparticles, 2 independent in vivo experiments were performed. For in vivo functional tests, sample sizes were 3, 4 or 5 for ENG or EMG recording of IT-IC interfacing so as to achieve statistical difference using ANOVA test.
Data exclusions	No data was excluded from the manuscript.
Replication	To ensure replication, all recording of ENG or EMG were repeated in 3-5 rats per group. For in vitro, ex vivo and in vivo experiments, all tests were repeated at least twice. The immunofluorescence staining images for infiltration of immune cells were obtained from the tissue of single rat, and biodistribution of gold nanoparticles was analyzed from the tissues of two rats. All attempts at replication were successful.
Randomization	No formal randomization was used but surgeries were carried out on groups.
Blinding	Investigators were blinded to group allocation during quantify the number of centronucleated myofibers, aspect ratio of myofibers, fibrotic tissue area, and the number of positive inflammatory cells. Blinding was not required for other study because the experimental group was only 'treated' one.

## Reporting for specific materials, systems and methods

We require information from authors about some types of materials, experimental systems and methods used in many studies. Here, indicate whether each material, system or method listed is relevant to your study. If you are not sure if a list item applies to your research, read the appropriate section before selecting a response.

## Materials &amp; experimental systems

## Methods

n/a	Involved in the study
<input type="checkbox"/>	<input checked="" type="checkbox"/> Antibodies
<input type="checkbox"/>	<input checked="" type="checkbox"/> Eukaryotic cell lines
<input checked="" type="checkbox"/>	<input type="checkbox"/> Palaeontology and archaeology
<input type="checkbox"/>	<input checked="" type="checkbox"/> Animals and other organisms
<input checked="" type="checkbox"/>	<input type="checkbox"/> Clinical data
<input checked="" type="checkbox"/>	<input type="checkbox"/> Dual use research of concern
<input checked="" type="checkbox"/>	<input type="checkbox"/> Plants

n/a	Involved in the study
<input checked="" type="checkbox"/>	<input type="checkbox"/> ChIP-seq
<input checked="" type="checkbox"/>	<input type="checkbox"/> Flow cytometry
<input checked="" type="checkbox"/>	<input type="checkbox"/> MRI-based neuroimaging

## Antibodies

Antibodies used	<p>Primary antibodies: CD11b Monoclonal antibody (M1/70) (47-0112-82, Invitrogen); Anti-Laminin antibody produced in rabbit (L9393, Sigma); F4/80 Monoclonal Antibody (BM8) (12-4801-82, Invitrogen); FITC anti-mouse CD8a Antibody (53-6.7) (100706, Biolegned); CD3e Monoclonal Antibody (145-2C11) (17-0031-82, Invitrogen).</p> <p>Secondary antibodies: Alexa Fluor 488 labeled goat anti-rabbit IgG (H+L) cross-adsorbed secondary antibody (A-11008, Invitrogen).</p>
Validation	<p>All antibodies are commercially available and have been tested by the manufacturer. Vendors and catalog numbers are listed above and validation can be found there.</p> <p>CD11b Monoclonal antibody (M1/70) (47-0112-82, Invitrogen): This monoclonal antibody recognizes CD11b. Manufacturer-validated to react with Mouse (<a href="https://www.thermofisher.com/antibody/product/CD11b-Antibody-clone-M1-70-Monoclonal/47-0112-82">https://www.thermofisher.com/antibody/product/CD11b-Antibody-clone-M1-70-Monoclonal/47-0112-82</a>).</p> <p>Anti-Laminin antibody produced in rabbit (L9393, Sigma): This polyclonal antibody recognizes Laminin. Manufacturer-validated to react with Human, Mouse (<a href="https://www.sigmaaldrich.com/KR/ko/product/sigma/l9393">https://www.sigmaaldrich.com/KR/ko/product/sigma/l9393</a>).</p> <p>F4/80 Monoclonal Antibody (BM8) (12-4801-82, Invitrogen): This monoclonal antibody recognizes F4/80. Manufacturer-validated to react with Mouse (<a href="https://www.thermofisher.com/antibody/product/F4-80-Antibody-clone-BM8-Monoclonal/12-4801-82">https://www.thermofisher.com/antibody/product/F4-80-Antibody-clone-BM8-Monoclonal/12-4801-82</a>).</p> <p>FITC anti-mouse CD8a Antibody (53-6.7) (100706, Biolegned): This monoclonal antibody recognizes CD8a. Manufacturer-validated to react with Mouse (<a href="https://www.biolegend.com/en-gb/products/fitc-anti-mouse-cd8a-antibody-153">https://www.biolegend.com/en-gb/products/fitc-anti-mouse-cd8a-antibody-153</a>).</p> <p>CD3e Monoclonal Antibody (17-0031-82, Invitrogen): This monoclonal antibody recognizes CD3. Manufacturer-validated to react with Mouse (<a href="https://www.thermofisher.com/antibody/product/CD3e-Antibody-clone-145-2C11-Monoclonal/17-0031-82">https://www.thermofisher.com/antibody/product/CD3e-Antibody-clone-145-2C11-Monoclonal/17-0031-82</a>).</p>

## Eukaryotic cell lines

Policy information about [cell lines and Sex and Gender in Research](#)

Cell line source(s)	HT-22 mouse hippocampal neuronal cell line (ATCC, Manassas, VA, USA); PC12 neuronal cell line (CRL-1271, ATCC)
Authentication	Cell lines were authenticated by the manufacturer by which the cells were received. The morphology of each cell (HT22 and PC12) was also confirmed by optical microscopy before use.
Mycoplasma contamination	All cell lines used in this work have been tested for mycoplasma infection every month and before in vitro experiments using mycoplasma detection kit (MycStrip, InvivoGen). All cell lines were not contaminated with mycoplasma.
Commonly misidentified lines (See <a href="#">ICLAC</a> register)	The cell lines used in this study are NOT present in the ICLAC register.

## Animals and other research organisms

Policy information about [studies involving animals](#); [ARRIVE guidelines](#) recommended for reporting animal research, and [Sex and Gender in Research](#)

Laboratory animals	Sparague Dawley rat (DBL, Cheongju, Republic of Korea), 300-350 g body weight, male, 10-12 weeks
Wild animals	Wild animals were not used in this study.
Reporting on sex	None.
Field-collected samples	The study did not involve field-collected samples.
Ethics oversight	The Sungkyunkwan University Institutional Animal Care and Use Committee approved the protocols used. (Approval No. SKKUIACUC2021-03-28-1 and SKKUIACUC2022-08-36-2)

Note that full information on the approval of the study protocol must also be provided in the manuscript.